Planetary and Space Science 179 (2019) 104741

Contents lists available at ScienceDirect

Planetary and Space Science

journal homepage: www.elsevier.com/locate/pss

Composition, mineralogy and chronology of mare basalts and non-mare materials in Von Kármán crater: Landing site of the Chang'E−4 mission

Zongcheng Ling [a,b,*], Le Qiao [a,**], Changqing Liu [a], Haijun Cao [a], Xiangyu Bi [a], Xuejin Lu [a], Jiang Zhang [a], Xiaohui Fu [a], Bo Li [a,c], Jianzhong Liu [d]

[a] Shandong Provincial Key Laboratory of Optical Astronomy and Solar-Terrestrial Environment, Institute of Space Sciences, Shandong University, Weihai, 264209, China
[b] Center for Excellence in Comparative Planetology, Chinese Academy of Sciences, Hefei, 230026, China
[c] College of Geoexploration Science and Technology, Jilin University, Changchun, 130026, China
[d] Institute of Geochemistry, Chinese Academy of Sciences, Guiyang, 550002, China

ARTICLE INFO

Keywords:
Moon
Chang'E−4
Von Kármán crater
Mare volcanism
Nonmare materials
Lunar exploration

ABSTRACT

As the first lunar farside landed mission, China's Chang'E−4 (CE-4) has safely landed on the volcanically resurfaced floor of Von Kármán crater in South Pole-Aitken (SPA) basin. The CE-4 mission will conduct rover exploration by Yutu-2 similar to what Chang'E−3 did in the northern Imbrium basin. Here we present a comprehensive study of the composition, mineralogy, and chronology of the basaltic and nonmare units in this crater, with the intent to provide context for the compositional properties of the landing site. Compositional maps (FeO, TiO_2, Mg#, and Th) demonstrate the heterogeneous distribution of mare and nonmare materials. Using a spectral survey of 1899 small impact craters (<1 km in diameter), we present a mineral map of high-Ca to low-Ca pyroxene ratio that is useful to untangle the effects of spectral mixing of these materials. Mare basalts with low-Ti composition and model ages of ~3.7 Ga and ~3.6 Ga have distinct mineral compositions that differ from the Chang'E−3 landing site, including no olivine enrichment. The non-mare materials have Mg-rich pyroxene, and Finsen crater materials (and Finsen ejecta) have higher Ca/Fe ratios than other parts of the rim of Von Kármán crater, indicating compositional anomaly of the SPA basin. The Von Kármán mare basalts show obvious compositional heterogeneity and complicated mixing effects with non-mare ejecta from subsequent impacts (e.g., the Eratoshenian-aged Finsen impact). We also present a geological map of the landing site, which reveals the geologic history of the landing region and will help to guide the surface exploration route of the CE-4's Yutu-2 rover. We also put forward some science questions to be answered by Yutu-2, to aid mission planning and scientific research.

1. Introduction

The enormous SPA basin is generally regarded as the largest (Wilhelms, 1987; Head et al., 1993; Garrick-Bethell and Zuber, 2009) and oldest impact basin (older than 4 Ga; e.g., Fassett et al., 2012) recognized on the Moon. Von Kármán crater (centered at 44.45°S, 176.3°E; diameter: 186 km) is a degraded Nectarian or pre-Nectarian impact crater, flooded with mare basalt units on the floor (Stuart-Alexander, 1978; Yingst et al., 2017; Pasckert et al., 2018). January 3, 2019, China's Chang'E−4 (CE-4) spacecraft, consisting of a lander and rover (Yutu-2) safely landed on the lunar farside, i.e., the scheduled landing site of the Von Kármán crater in the South Pole-Aitken (SPA) basin (Wu et al., 2017; Huang et al., 2018). After landing, CE-4 released the Yutu-2 rover to traverse around and perform detailed geologic investigations. Surface *in-situ* exploration missions (e.g., CE-4) into the central portion of SPA basin have great potential to advance scientific understanding in key areas including knowledge of very large impact basin formation processes, late heavy bombardment history of the Earth-Moon system, composition of the lower crust and possibly upper mantle, and lateral and vertical compositional diversity of the lunar interior (Duke et al., 2000; National Research Council, 2007; Jolliff et al., 2017).

Here we report the geologic context, spectroscopic, compositional

* Corresponding author. Shandong Provincial Key Laboratory of Optical Astronomy and Solar-Terrestrial Environment, Institute of Space Sciences, Shandong University, Weihai, 264209, China.
** Corresponding author.
E-mail addresses: zcling@sdu.edu.cn (Z. Ling), leqiao.geo@gmail.com (L. Qiao).

https://doi.org/10.1016/j.pss.2019.104741
Received 8 February 2019; Received in revised form 9 September 2019; Accepted 9 September 2019
Available online 10 September 2019
0032-0633/© 2019 Elsevier Ltd. All rights reserved.

and chronological investigations of the mare basalt and nonmare units in Von Kármán crater, with an intent to recognize their scientific potential from a remote sensing view, which should be better understood during the CE-4 mission's operations. In this study, we provide geologic context for the landing site within Von Kármán crater, focusing on the mineralogical and compositional properties of the mare basalts and nonmare materials that occur in the region of the CE-4 lander and rover. The geologic map and compositional studies provide critical constraints and guidance for the CE-4 Visible-Near Infrared Spectrometer (VNIS) and Lunar Ground Penetration Radar (LPR) studies in early 2019. We also provide context for science questions to be answered by Yutu-2, to aid mission planning and scientific research.

2. Data and methods

We employ the Chang'E−1 CCD images (120 m/pixel), Lunar Reconnaissance Orbiter Camera (LROC) Wide Angle Camera (WAC) mosaic (100 m/pixel) for regional geologic context and geomorphological analyses (Li et al., 2010; Robinson et al., 2010) to give the geologic context, geomorphology of SPA basin, Von Kármán crater and the CE-4 landing site. Topographic information of the studied region is derived from the merged digital elevation model (DEM) that is derived from the LRO Lunar Orbiter Laser Altimeter (LOLA; Smith et al., 2010) and Kaguya Terrain Camera (TC) data (SLDEM: 59 m/pixel; Barker et al., 2016). We produced a slope map for the CE-4 landing region using SLDEM topography at a baseline of ~180 m. Detailed results are given in section 3 and Figs. 1–2.

To evaluate the compositional properties of the mare basalts in Von Kármán crater, we use Kaguya Multi-band Imager (MI) data (20 m/pixel; Ohtake et al., 2010) to map the TiO_2 and FeO distributions in Von Kármán crater with algorithms from Otake et al. (2012) and Lemelin et al. (2015), respectively. Those algorithms are derived based on the "ground truth" from returned Apollo and Luna samples, in combination with the multispectral imaging data sets of corresponding sampling sites. They are as follows:

$$TiO_2\ (\text{wt. }\%) = 0.72 \times \theta_{Ti}^{14.964} \quad (1)$$

$$\theta_{Ti} = \arctan(((R_{415}/R_{750})\text{-}0.208)/(R_{750}+0.108)) \quad (2)$$

$$FeO\ (\text{wt. }\%) = (1.0708 \times \theta_{Fe2})\text{-}0.3986 \quad (3)$$

$$\theta_{Fe2} = 0.0656e^{(3.6681\times\theta Fe1)} \quad (4)$$

$$\theta_{Fe1} = \text{-}\arctan(((R_{950}/R_{750})\text{-}1.39)/(R_{750}\text{-}0.04)) \quad (5)$$

The Mg# (mole percent MgO/(MgO + FeO)) map of the region is derived from Chang'E−1 Imaging Interferometer (IIM; 200 m/pixel) data. Similar to the methods of FeO and TiO_2 mapping using Kaguya MI data, we employ Mg# for Apollo and Luna sample analyses as ground truth to map Mg#. The IIM data was binned into 4 × 4 pixels to suppress the random noise and improve the signal-to-noise ratio. Thorium (Th) content distribution map of the CE-4 landing site from Lunar Prospector has a spatial resolution of 0.5°/pixel from Lunar Prospector data (Prettyman et al., 2006). Detailed results are given in section 4 and Fig. 3.

We use orbital hyperspectral imaging data from Chandrayaan-1 Moon Mineralogy Mapper (M^3) data (Green et al., 2011) to evaluate the spectral and mineralogical variations of the mare units and the nonmare materials. Moon Mineralogy Mapper (M^3), a guest payload on Chandrayaan-1, has been employed to detect lunar global and regional mineralogy with high spatial and spectral resolution (Green et al., 2011; Boardman et al., 2011). We select ten scenes M^3 data that are of optical period OP2C according to the range of Von Karman in the NASA PDS Geosciences Node (http://ode.rsl.wustl.edu/). OP2C data is collected with a spatial resolution of ~280 m/pixel at a spacecraft altitude of ~200 km (Cheek et al., 2011). Ground truth value correction and geometry correction are employed on the data. We then mosaic all the M^3 data (Table 1) to give a full view of the Von Karman crater. We acquired the spectra of small craters with average values of 2 × 2 pixels. All the spectra extracted are only shown from a single optical period (OP2C) for direct spectral comparisons. The spectra are smoothed by Savitzky-Golay (SG) convolution method. The continuum of each individual spectrum is

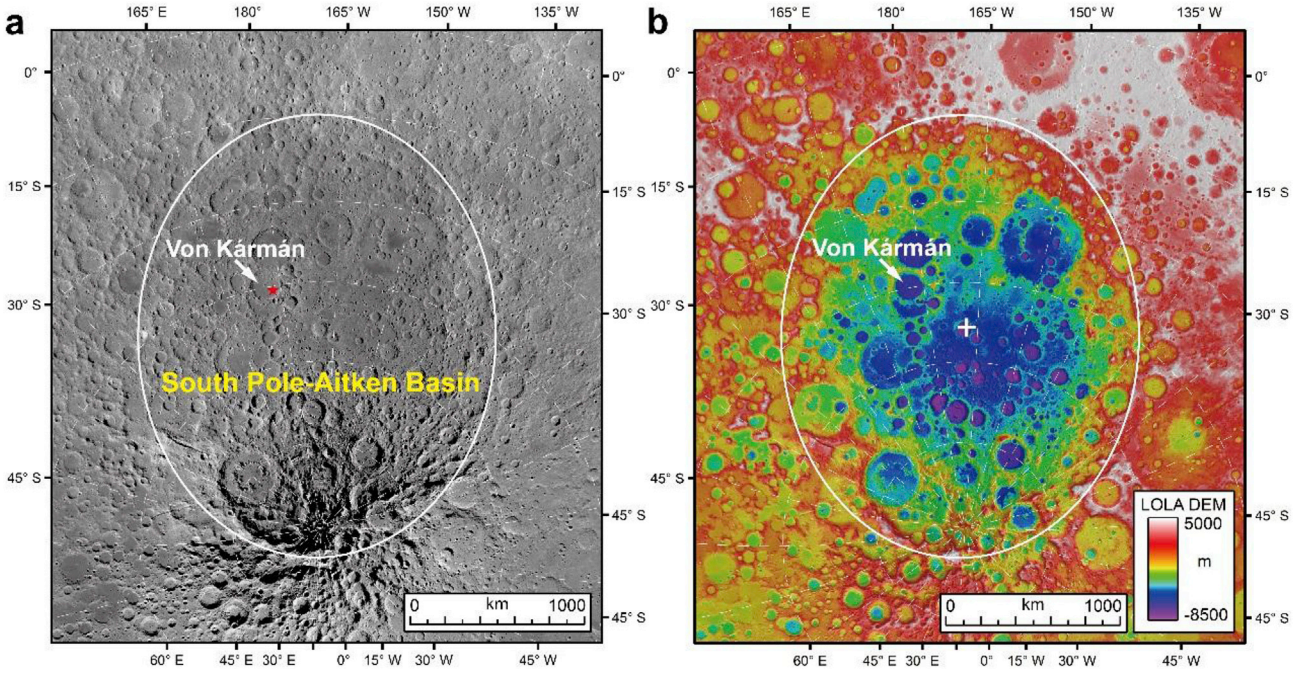


Fig. 1. The context of Von Kármán crater within the South Pole-Aitken (SPA) basin. (a) LROC WAC image mosaic and (b) LOLA DEM topography (128 pixel/degree) overlaid on WAC images. The white outline in panels (a) and (b) represents the outer ellipse of SPA basin. The location of Von Kármán crater is pointed out by the white arrow. The Chang'E−4 landing site is shown by the red star. The white cross marks in (b) the ellipse center of SPA basin (Garrick-Bethell and Zuber, 2009). The projections are stereographic centered at 191°E, 53°W, and north is up. (For interpretation of the references to color in this figure legend, the reader is referred to the Web version of this article.)

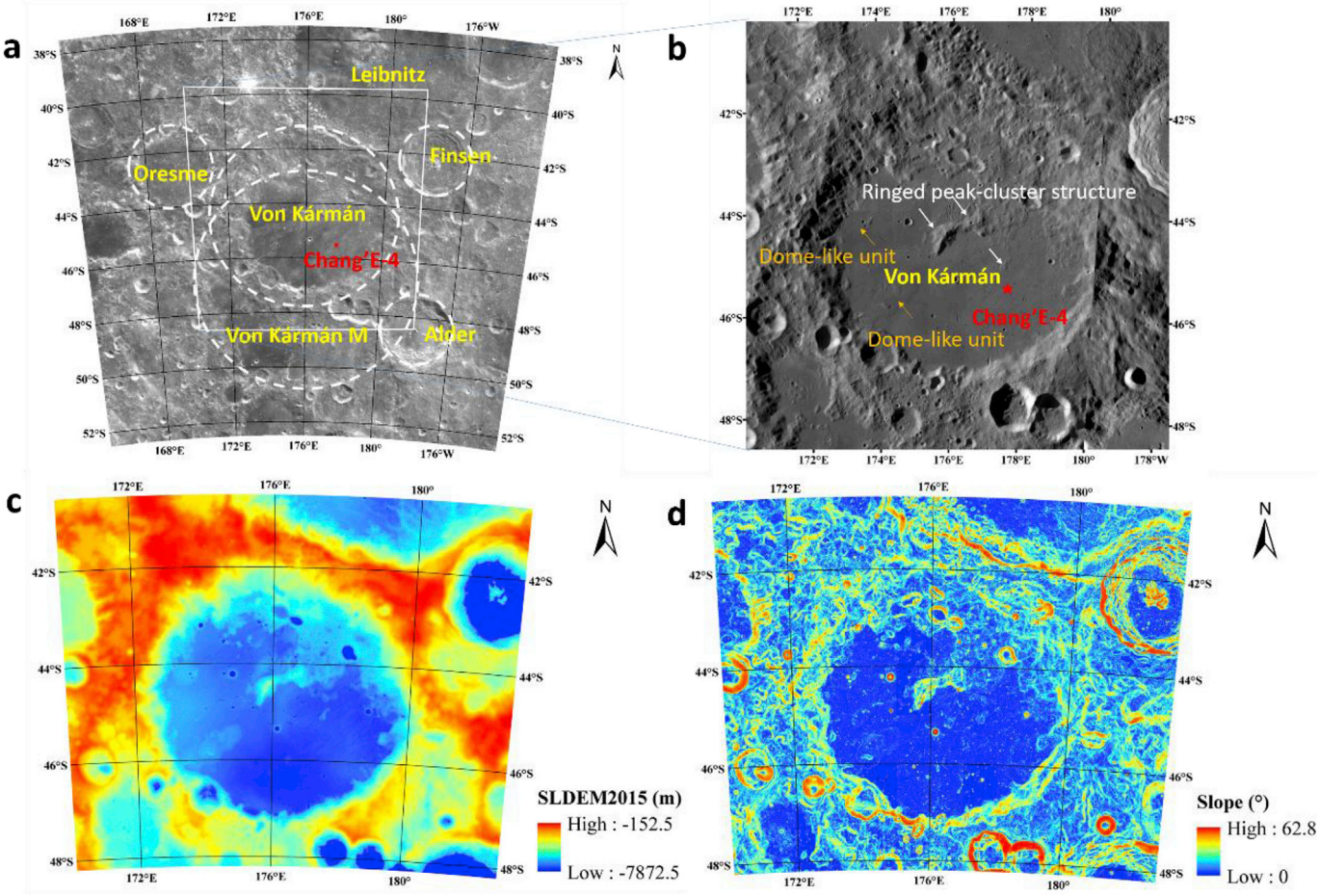


Fig. 2. The regional context of Von Kármán crater. (a) Chang'E−1 CCD image; (b) LROC WAC image, the three white arrows point to the ringed peak-cluster and the two white arrows point to the dome-like structures, respectively; (c) SLDEM2015 topography (~60 m horizontal resolution) overlaid on LOLA shaded relief image. (d) SLDEM2015-derived slope map (baseline ~180 m) overlaid on LOLA shaded relief image. The dotted white circles in panel (a) marks the rim locations of Von Kármán, Von Kármán M, Finsen, Alder, and Oresme craters.

removed using two straight lines with three points defined by the local maximum reflectance between 0.66~0.91 μm and 1.35~1.82 μm, and the right endpoint position at 2.62 μm. Continuum removal of the spectra lead to more prominent absorption features to help identify the mineral chemistries.

Integrated Band Depth (IBD) is a useful parameter to evaluate the properties of the whole absorption band of mafic minerals. Following the method by Thiessen et al. (2014), we created color composite images using IBD1000 (red channel, IBD from 789 to 1308 nm), IBD2000 (green channel, IBD from 1658 to 2458 nm) and R750 (blue channel, reflectance of 750 nm). Note that here we use the reflectance of 750 nm instead of the reflectance of 1589 nm of the M^3 science team (e.g., Besse et al., 2011) for the blue channel due to its limited absorptions of mafic minerals at 750 nm (Thiessen et al., 2014). On the contrary, the 1250 nm absorption feature of plagioclase and 2000 nm absorption feature of low-Ca pyroxene may affect the 1589 nm reflectance from their end-member spectra (Fig. 1 from Pieters et al., 2014). In order to evaluate the spatial variations of mineralogy in Von Kármán crater, we conduct a systematic spectral survey of small, fresh craters superposed on the basaltic and nonmare units. We collect spectra of 1899 small craters less than 1 km in diameter, which present fresh materials with sharp spectral absorption peaks. We estimate the mineral modes of these spectra using the Modified Gaussian Model (MGM) deconvolution method (Sunshine and Pieters, 1993, 1998). Detailed results are given in section 5 and Figs. 4–5.

We estimate the absolute model ages of mare basaltic units and Finsen crater using crater size-frequency distribution (CSFD) measurements. We count all superposed impact craters ≥200 m in diameter using the CraterTools extension in ESRI's ArcGIS environment (Kneissl et al., 2011) on Kaguya TC images (~10 m/pixel). During the crater counting investigations, special care has been taken to eliminate contamination by secondary impact craters and endogenous pits according to their morphologic characteristics (e.g., Shoemaker, 1962; Oberbeck and Morrison, 1974). We calculate absolute model ages by fitting the crater counting results on the basis of the lunar chronology function (CF) and production function (PF) of Neukum et al. (2001) using CraterStats software (Michael and Neukum, 2010; Michael et al., 2016). Detailed results are given in section 6 and Fig. 6.

3. Geologic context of Von Kármán crater

The Von Kármán crater is centered at 44.45°S, 176.25°E (based on LOLA 2011 control network), located in the central region of SPA basin (Fig. 1). The exact landing site of CE-4 has been confirmed by multi-source data (e.g., digital orthophoto map of Chang'E−2, LROC NAC images, CE-4 descent camera images and monitoring camera images) and is given as the red star in Fig. 1 at 45.457°S, 177.588°E (Di et al., 2019). The Von Kármán crater shows degraded topographic and morphologic patterns, and geological mapping studies have designated it as a Nectarian-aged or pre-Nectarian crater (Stuart-Alexander, 1978; Yingst et al., 2017).

Regionally, the Von Kármán crater is encircled by several other post-

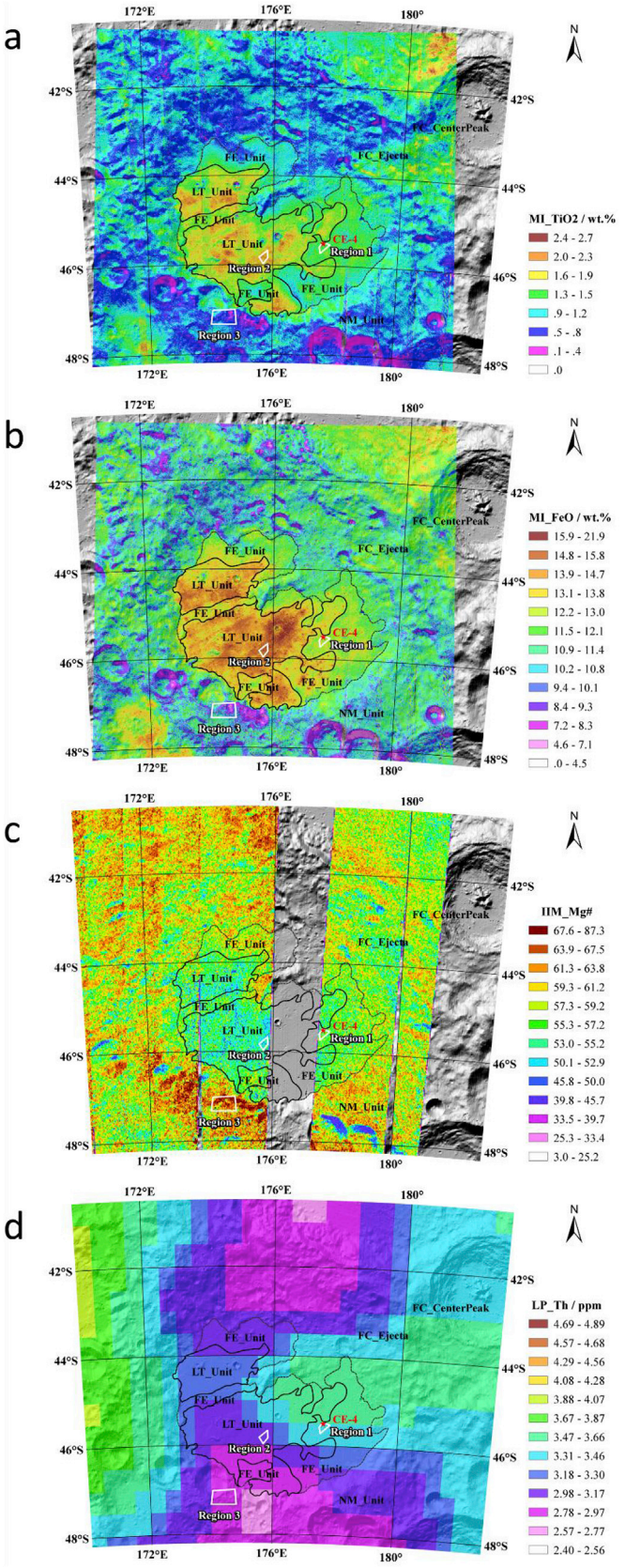


Fig. 3. Chemical compositions of Von Kármán crater. (a) TiO_2 map and (b) FeO map using Kaguya Multiband Imager (MI) data, (c) Mg# (100 × MgO/(MgO + FeO)) map using Chang'E−1 IIM data, and (d) Th maps from Lunar Prospector data. The basemap is LOLA shaded relief image. Black polygons are the unit division results: LT: low-titanium mare unit, FE: Finsen ejecta unit.

SPA impact basins and craters; these basins/craters have complex stratigraphic relationships (Fig. 2a and b; Qiao et al., 2019). The Von Kármán crater clearly superposes (and is thus younger than) the pre-Nectarian Von Kármán M cater. Geomorphologic investigations show the northern portion of the rim structures of Von Kármán M crater has been largely obliterated and buried during the Von Kármán impact event. The Von Kármán M crater has an estimated diameter of ~245 km (Head et al., 2010). A much larger impact crater, Leibnitz, with a diameter of ~240 km, lies very close to the north rim of Von Kármán crater. It appears that this larger crater postdates Von Kármán crater, and the rugged and knobby terrains of the northern interior of Von Kármán are probably ejecta deposits from the Leibnitz impact crater.

The most prominent large impact crater in the regional context is the 73-km-diameter Finsen crater to the northeast of Von Kármán crater. Earlier geologic mapping has interpreted it as an Eratosthenian-aged crater (Stuart-Alexander, 1978). On optical images and reflectance maps, extensive ray patterns and secondary craters radial to Finsen crater center are clearly observed. Imaging spectrometer mapping analyses show that, however, these bright ray patterns are mainly due to the compositional difference between highlands-rich Finsen ejecta (brighter) and local mare basalts (darker), not due to the presence of fresh, high-albedo materials (Hawke et al., 2004). Thus, these ray patterns associated with Finsen crater are probably not reliable indications for the Copernian crater ages (Hawke et al., 2004). In addition, Finsen is also not registered as a Copernian crater by several prior investigations (Werner and Medvedev, 2010; Ravi et al., 2016; Mazrouei et al., 2019). The mare deposits within Von Kármán are also extensively overprinted by ejecta materials from the Finsen crater (Pasckert et al., 2018) (see more in sections 4-5).

Von Kármán crater is 186 km in diameter and the crater floor is ~3.5 km below the rim crest (Fig. 2c). This crater shows degraded rim, wall terraces and ejecta terrains, and no solidified impact melts have been definitely identified in the crater interior and adjacent exterior; all these degraded morphological characteristics reflect several billion years of topographic degradation processes and volcanic resurfacing after the crater formation. High-resolution LRO altimetry and image data show this basin probably developed a peak-ring or peak-cluster structure (poorly preserved) (Fig. 2b), resembling central structures observed in other peak-ring and peak-cluster basins on the Moon (Baker et al., 2011).

The Von Kármán crater interior floor is characterized by a wide range of geomorphologies and shows a distinct dichotomy between the northern and the southern portions (Fig. 2b). The northern crater interior is dominated by ejecta deposits, with rugged surface textures (Fig. 2b) and a feldspar-dominated composition that is more mafic than typical lunar highlands (10–14 wt% FeO, using Clementine UV-VIS-derived FeO (Lucey et al., 2000). The southern portion of the crater interior is largely filled with mare lava deposits, characterized by a relatively flat surface (Fig. 2d) and an FeO-rich basaltic composition (13–18 wt% FeO; Fig. 3b). These mare plains occupy an area of 1.063×10^4 km^2. Topographic elevations (Fig. 2c) of the mare lava plain mainly range from approximately −5600 to −6000 m (relative to the mean planetary radius), and the western part is generally higher than the southern part, which shows a topographic decline of ~350 m across a distance of ~80 km. Two bulge- or dome-like structures, ~15–40 km in diameter and up to ~350 m high, occur in the western margin of the interior mare units (Pasckert et al., 2018), which may represent the source vent areas for the later volcanic flows in the western Von Kármán floor.

4. Chemical compositional properties of mare basalts and surrounding non-mare materials

As shown in Fig. 3a and b, many fresh craters excavated relatively FeO- and TiO_2-richer underlying basaltic materials than those of surface materials, indicating heavy reworking and impact gardening of the surface basaltic materials. The contamination and mixing of Finsen ejecta with local mare materials is evident by light-colored linear patterns

Table 1
Information of Moon Mineralogy Mapper (M^3) datasets used in this study.

Data File Name	Date	Optical Period	Orbit Altitude(km)	Resolution(m/pixel)
M3G20090622T082242_V01_RFL	2009/6/22	OP2C	200	280
M3G20090622T124051_V01_RFL	2009/6/22	OP2C	200	280
M3G20090623T012541_V01_RFL	2009/6/23	OP2C	200	280
M3G20090719T160300_V01_RFL	2009/7/19	OP2C	200	280
M3G20090719T200620_V01_RFL	2009/7/19	OP2C	200	280
M3G20090720T003411_V01_RFL	2009/7/20	OP2C	200	280
M3G20090720T043741_V01_RFL	2009/7/20	OP2C	200	280
M3G20090720T090521_V01_RFL	2009/7/20	OP2C	200	280
M3G20090816T005433_V01_RFL	2009/8/16	OP2C	200	280
M3G20090816T045833_V01_RFL	2009/8/16	OP2C	200	280

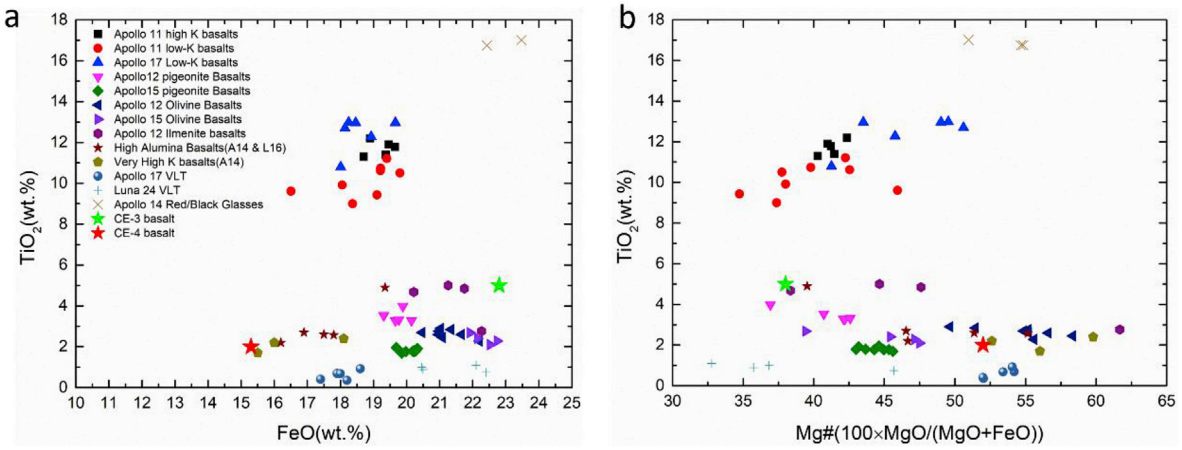


Fig. 4. Comparison of chemical variations between Chang'E-4 mare basalt and other mare basalts of Apollo and Luna samples (Papike et al., 1998) as well as Chang'E-3 mare basalt (Ling et al., 2015). (a) FeO versus TiO_2; (b) Mg# (100 × MgO/(MgO + FeO)) versus TiO_2.

(Fig. 2a) with relatively low FeO and TiO_2 values pointing toward Finsen crater (Fig. 3 a,b). Using TiO_2 content as the discriminator for lava units, we divide the mare region in Von Kármán crater into two units, i.e., Low-Ti unit (LT, 3 wt % > TiO_2 > 1.5 wt %) and Finsen ejecta unit (FE, TiO_2 < 1.5 wt %), as shown by the polygons in Fig. 3.

Except mare basalts in the Von Kármán crater, the nonmare materials are ubiquitous from nearby terrains of SPA interior floors, which are derived from SPA impact event rather than the later mare volcanisms that formed the mare basalts. For those nomare materials (NM units) surrounding the mare basalts in Von Kármán crater, we find they generally have lower FeO and TiO_2 contents, except for the ejecta of Finsen crater, which seems to be slightly richer in FeO and TiO_2 than other nonmare regions (Fig. 3a and b). The Mg# (mole percent MgO/(MgO + FeO)) map (Fig. 3c) derived from Chang'E−1 Imaging Interferometer (IIM) data provide the detailed heterogeneous Mg# distribution of this region. We find that the nonmare materials from Finsen impact ejecta and Von Kármán crater rim (represented by Regions 1 and 3 in Fig. 3, which include the Chang'E−4 landing site) are slightly more magnesian (Mg# = ~56 ± 2 for Region 1 and Mg# = ~64 ± 4 for Region 3) than the mare materials (represented by Region 2 in Fig. 3, Mg# = ~52 ± 2). Lunar Prospector gamma-ray data for Th (Fig. 3d) (Prettyman et al., 2006) indicates that the ejecta of Finsen crater has a higher Th content (~3.6 ppm) than that of mare basalts (~2.8 ppm).

The mare surface in Von Kármán crater is relatively low in FeO (~13–18 wt %) and TiO_2 (~1–3 wt %) in comparison with basalt at the Chang'E−3 landing site (i.e., ~22.8 wt % FeO and ~5.0 wt % TiO_2) (Ling et al., 2015). It is clear that the typical mare basalt (Region 2) belong to a low-Fe (15.3 ± 0.6 wt%) and low-Ti (2.0 ± 0.3 wt%) endmember, while the Mg composition suggest they are relatively high in Mg# values (~52 ± 2). Compared to the various mare basalt types of Apollo and Luna samples (Fig. 4), CE-4 mare basalt stands out as a special type of basalt with similar Fe, Ti contents and Mg# values with the very high K basalt and high aluminum basalt from Apollo 14 (e.g., Apollo 14053, 14168, 14305, 14321 samples) and Luna 16 missions. The characteristic chemical compositions of CE-4 basalt may imply a unique view of farside volcanism.

5. Spectral properties and mineralogical composition

As shown in Fig. 5a, mare basaltic materials show hues between yellow and red, indicating they are rich in mafic minerals. Ejecta from Finsen crater make the mixed mare materials appear bluish in color, suggesting the contamination of feldspathic materials. We select seven small, fresh craters or steep slopes (coordinates of locations are given in Table 2) with sharp spectral features among different units as shown in Fig. 5b, and extract their spectra. As shown in Fig. 5c and d, we find that the LT unit generally has longer 1 and 2 μm absorption centers than those of the FE unit, indicating the existence of more Ca- and Fe-rich pyroxenes. The central peak of Finsen crater shows its characteristic spectral absorption features approaching ~900 nm and ~1900 nm, indicating more magnesian compositions than its ejecta (i.e., FC_ejecta, blue line), consistent with the findings of Moriarty and Pieters (2018). Similarly, nonmare material also show spectral features, indicating a more Mg-rich composition of the pyroxene.

The result of spectral survey of small craters suggests that the LT unit has more high-Ca pyroxene (HCP) relative to low-Ca pyroxene (LCP) than the FE unit. We calculate the mineral absorption centers using MGM, which present quantitative mineralogy information than conventional spectral profile analyses. The spatial distribution of these results is given in Fig. 6a. The volume percentage ratio of HCP and LCP (HCP/LCP) is estimated using their band-strength ratios of 1 and 2 μm bands from MGM deconvolution of M^3 spectra. Using a Kriging interpolation technique, we obtain the mineral (HCP/LCP ratio) map shown in Fig. 6b, which provides better discrimination of the compositional boundaries.

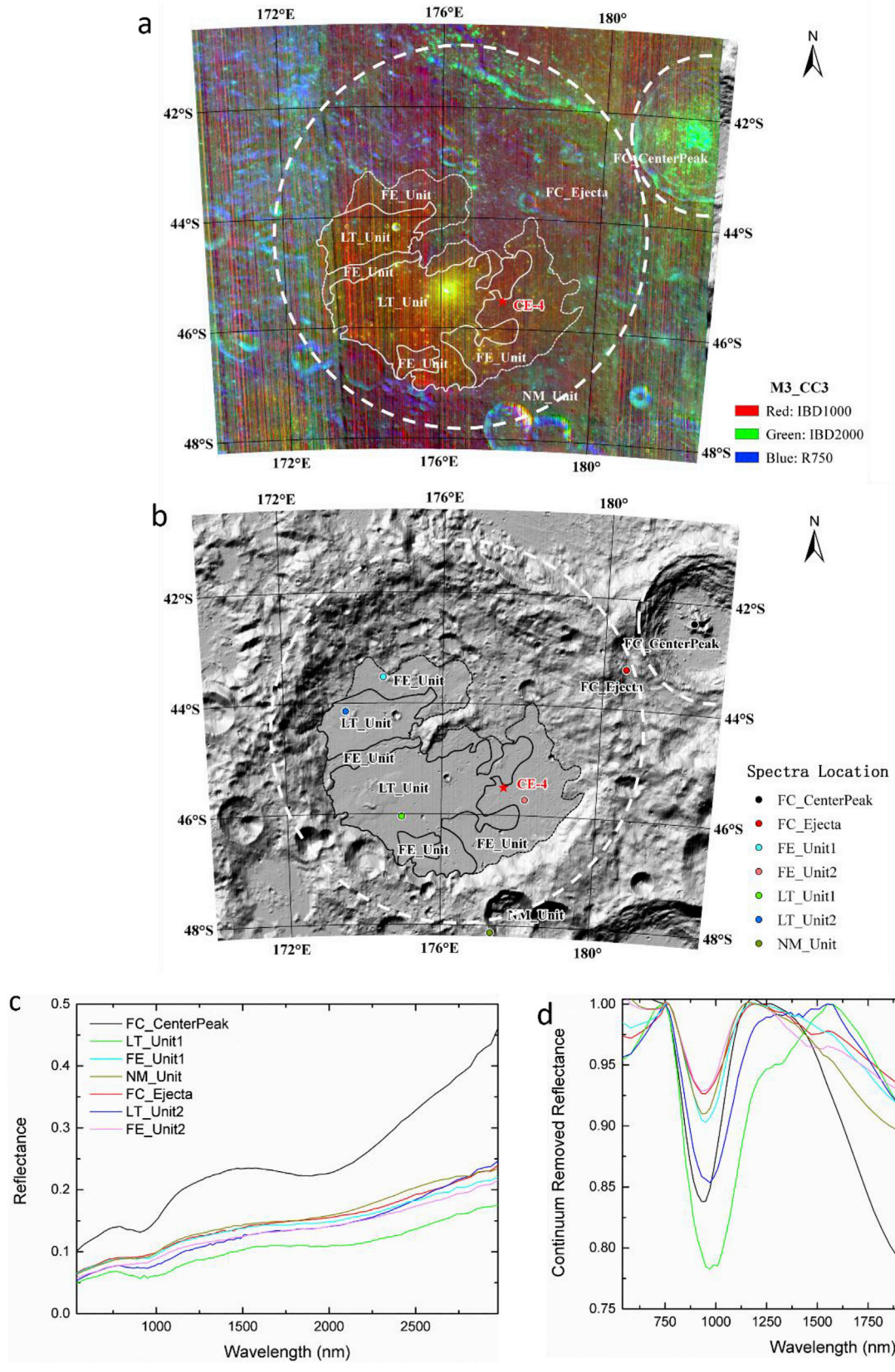


Fig. 5. Spectral characteristic of different units in the Von Kármán crater. (a) Color composite (CC) of M^3 data using IBD 1000, IBD 2000 and R750 nm; (b) Locations of representative spectra Von Kármán crater; (c) Representative spectra of Von Kármán crater; (d) Continuum-removed representative spectra of Von Kármán crater. Points in panel (b) indicate area where the representative spectra are taken out of LT, FE and nonmare (NM) units. The basemap is LOLA shaded relief image. (For interpretation of the references to color in this figure legend, the reader is referred to the Web version of this article.)

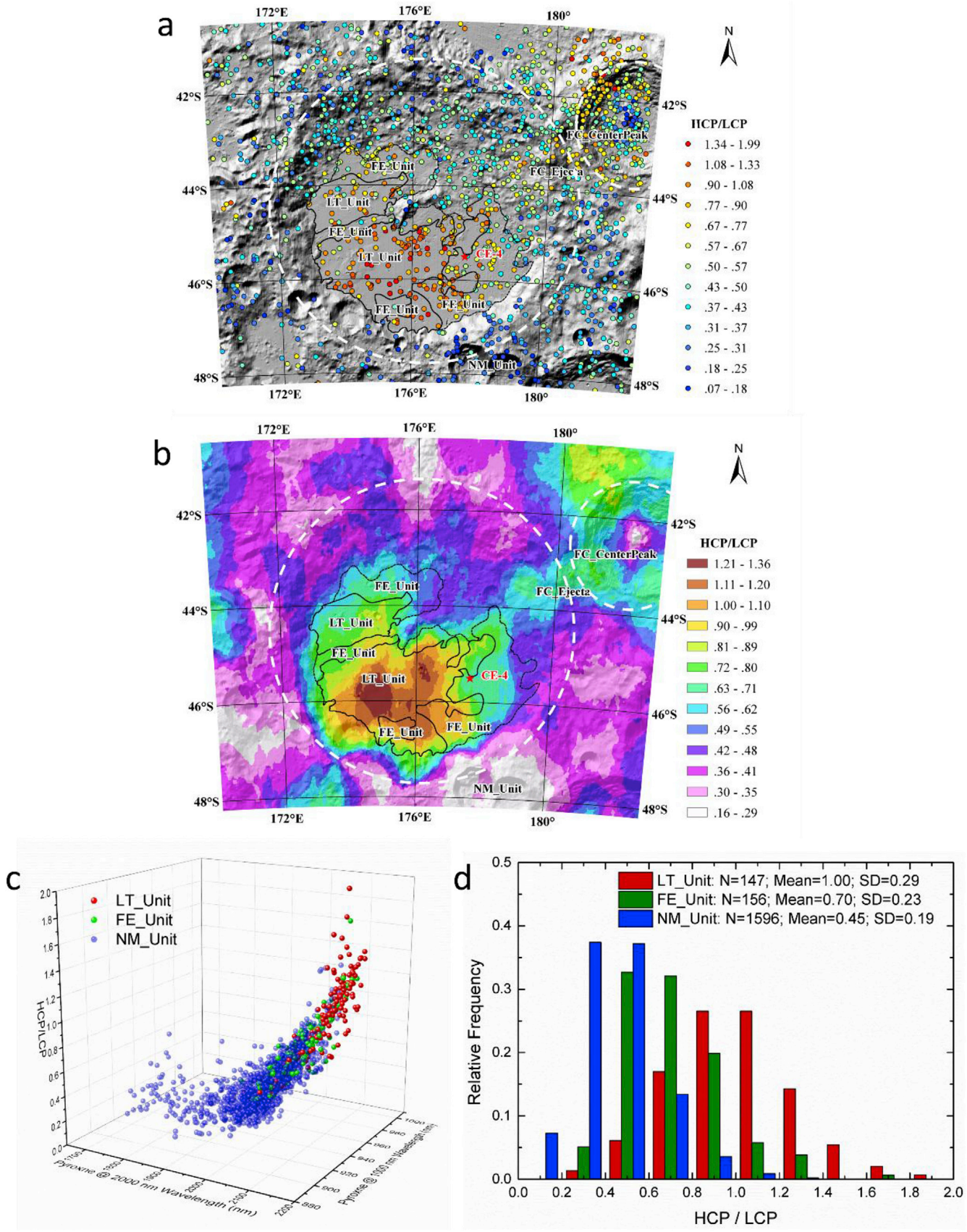


Fig. 6. Spectral survey of small craters of Von Kármán crater. (a) Mineral ratios of High-Ca pyroxene (HCP) and Low-Ca pyroxene (LCP) derived from MGM method; (b) Mineral map based on the interpolation of (a) using Kriging interpolation technique; (c) Pyroxene VNIS peak positions and HCP/LCP ratios of Von Kármán crater materials; (d) Histogram of HCP/LCP ratios derived from the spectral survey of small craters. The basemap in (a) and (b) is LOLA shaded relief image.

Table 2
Coordinates of locations of representative spectra in Von Kármán crater area.

Spectrum ID	Latitude (°)	Longitude (°)	Unit Name
Spec_01	−42.360178	182.133365	FC_CenterPeak
Spec_02	−43.283169	180.551836	FC_Ejecta
Spec_03	−46.046955	174.967225	LT_Unit1
Spec_04	−44.149121	173.561998	LT_Unit2
Spec_05	−43.532065	174.516101	FE_Unit1
Spec_06	−45.720279	178.145839	FE_Unit2
Spec_07	−48.131462	177.342111	NM_Unit

This mineral map has advantages of probing the subsurface mineral variations and minimizing the effects of impact mixing in the upper meter of soils (such as those obtained through optical spectroscopic and gamma-ray data as shown in Fig. 3). Clearly, the mare materials generally have the greatest HCP/LCP values, whereas the nonmare materials have low HCP/LCP values. As given by the 3D scatter plot of the results of the spectral survey (Fig. 6c), the LT unit has the longest 1 and 2 μm absorption feature, while the FE unit has intermediate compositional and spectral characteristics. Statistically, as shown in Fig. 6d, the LT units have a mean HCP/LCP value of 1.0, with a standard deviation of 0.29; the FE unit has a mean HCP/LCP value of 0.7, with a standard deviation of 0.23; the NM unit has a mean HCP/LCP value of 0.45, with a standard deviation of 0.19. The Finsen crater ejecta seems to expose more HCP/LCP elevated materials than its central peak, indicating a Fe/Ca rich nature of the upper layer of Finsen crater area. The different degree of mixing between Finsen ejecta and mare materials in Von Kármán crater lead to the intermediate HCP/LCP ratios. Interestingly, CE-4 just landed on the LCP rich region (HCP/LCP ~0.7), which is probably composed of a large amount of LCP-rich materials derived from Finsen crater ejecta and other impact events on nonmare regions of the Von Kármán crater. Huang et al. (2018) estimated the regolith thickness of the FE unit in LT units to be several meters. Lunar Penetration Radar (LPR) measurements by CE-4 will provide ground truth for this estimate, which will help to improve understanding of the gardening and evolution of lunar regolith.

As shown in Fig. 6a and b, the nonmare materials are generally Mg-rich for pyroxene. Specifically, pyroxene on the southern rim of Von Kármán crater is even more Mg-rich than those pyroxene in the ejecta of Finsen crater. This is consistent with the Mg# map (Fig. 3c) which showing the more Mg-rich southern rim of the crater than the Finsen ejecta and the mare basalts. Interestingly, the central peak of Finsen crater exhibits low HCP/LCP values, indicating a more Mg-rich pyroxene composition. The northern and southern rim of Von Kármán crater appear to expose more Mg-rich pyroxenes. This observation is consistent with Moriarty and Pieters (2018), who suggested the interior of SPA could be divided into three composition zones as SPA compositional anomaly (SPACA), Mg-Pyroxene Annulus, and Heterogeneous Annulus. According to Moriarty and Pieters (2018), Finsen crater and its ejecta belong to the SPACA unit, whereas other nonmare regions in Von Kármán crater belong to the Mg-Pyroxene Annulus. In addition, olivine was not observed in the spectral survey, in agreement with previous spectral studies of materials in SPA basin which is expected to have excavated the lunar upper mantle materials onto the surface (Yamamoto et al., 2012; Melosh et al., 2017), supporting the hypothesis that the lunar upper mantle was probably enriched in low-calcium pyroxene (LCP) but not olivine. As have been noted by Moriarty and Pieters (2018), the origin of Mg-rich pyroxene in SPA and the nature of unusual SPACA surface materials are unanswered questions which are keys for unraveling the complex geologic history of SPA basin. In this sense, Von Kármán crater is a good place to check the compositional and geologic differentiation of the SPA basin, if these relatively high Ca/Fe nonmare pyroxenes might be encountered by the CE-4 rover and detected with its VNIS payload.

In order to present detailed geological and compositional context and provide remote sensing observation constraints for Yutu-2 operations, we show a more close view of the Chang'E−4 landing site (Fig. 7). As shown

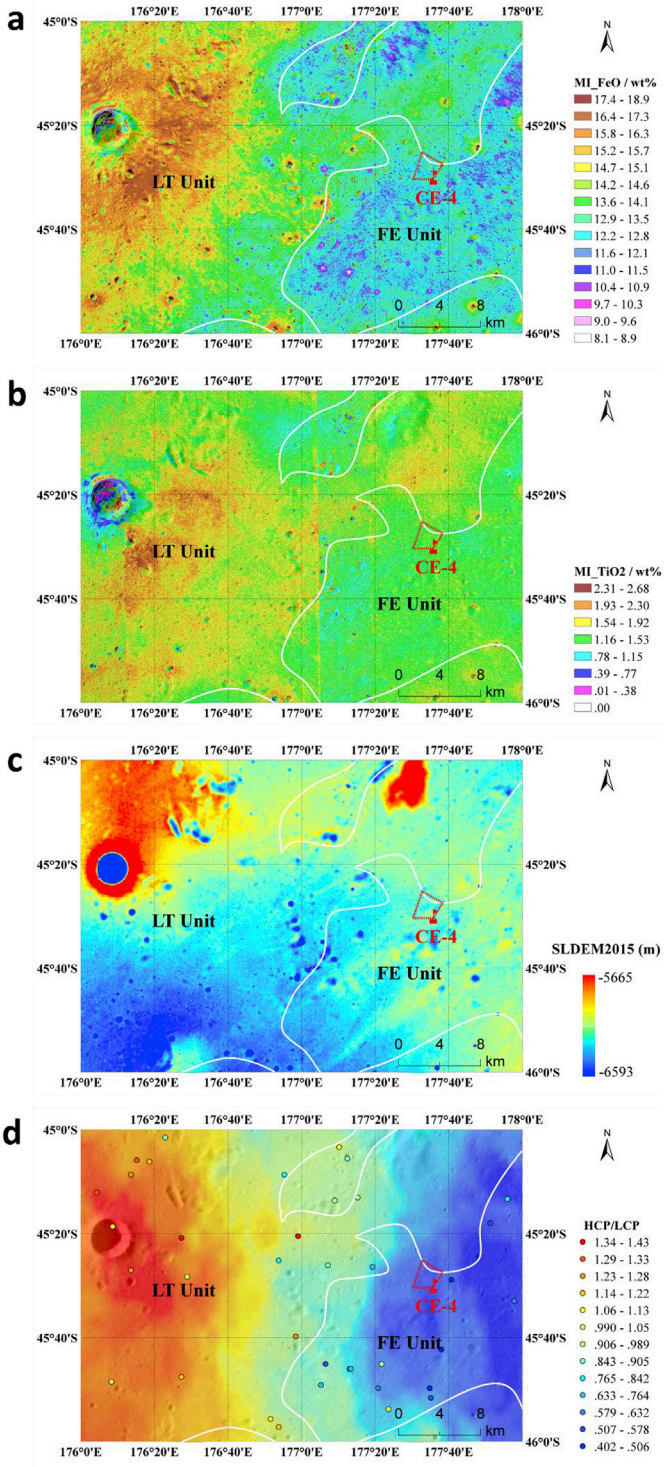


Fig. 7. Close view of Chang'E-4 landing site in Von Kármán crater. (a) FeO map; (b) TiO_2 map; (c) SLDEM2015 topography; (d) HCP/LCP mineral ratios.

in Fig. 7a and b, Von Kármán mare basalt is relatively low in FeO (~13–18 wt %) and TiO_2 (~1–3 wt %). Relatively FeO and TiO_2-rich underlying basaltic materials are exposed to surface, indicating the degree of regolith mixing and gardening are high. CE-4 landing area is a topographically very flat region on the mare plain (Fig. 7c), which is on an average elevation of −5928±6 m. As shown in Fig. 2d, the result suggests the LT basalt has more HCP relative to LCP than the FE unit. CE-4 just landed on the LCP rich region (HCP/LCP = ~0.7), which is probably composed of a large amount of LCP-rich materials derived from

Finsen crater ejecta and other impact events on nonmare regions of the Von Kármán crater.

6. Chronology of mare basalts

The chronology of Von Kármán crater basalts is conducted by CSFD using areas shown in Fig. 8a. We separate the LT region into two areas (Fig. 8a, LT_1 and LT_2) for age analysis according to their different mineral distributions (i.e., HCP/LCP) as indicated in Fig. 5b.

There are two previous chronological studies of mare basalts in Von Kármán crater floor using CSFD measurements. Haruyama et al. (2009) obtained a model age of 3.35 Ga for these mare deposits, whereas a recent study by Pasckert et al. (2018) derived an age of 3.15 Ga and inferred a buried lava flow to be 3.75 Ga old. Here we contribute to the chronological investigation using our updated mare basalt unit division (section 4). As shown in Fig. 8c, The CSFD curve of the LT_1 units is featured by an characteristic deflection (knee) at ~1 km diameter, which can be interpreted to the presence of two mare flow units separated in time: an older mare flow unit and a younger mare flow resurfacing unit (preferentially covering smaller craters (with crater depths smaller than the resurfacing flow thickness) and resulting in deficit of smaller crater) (Hiesinger et al., 2002). The age of LT_1 is determined to be ~3.38 ± 0.03 Ga by fitting craters from ~300 m to ~1 km in diameter for the younger resurfacing lava flows, similar to that of Haruyama et al. (2009), and the larger craters (>1 km) yield an age of ~3.72 Ga for the buried lava flows. The depth of craters (approximately 1/10 of the crater diameter; Melosh, 1989) of the deflection diameter (~1 km) can be used to constrain the depth of the older ~3.72 Ga buried lava flow, i.e., >100 m. The more recent volcanic event may have a higher HCP/LCP ratio than the earlier volcanic event (~3.72 Ga), indicating different composition of their mantle sources. The age of LT_2 (Fig. 8d) is determined to be ~3.57 (+0.07/-0.12) Ga by fitting craters >1.3 km. The Finsen crater has been dated to be ~3.6 Ga through crater population study of Finsen crater floors (Ivanov et al., 2018). However, this reported age will place Finsen even older than parts of the Von Kármán floor maria (3.35 Ga, Haruyama et al., 2009; 3.15 Ga, Pasckert et al., 2018; 3.38 Ga, this study), which is in consistent with the pervasively observed superposition of Finsen ejecta materials on the Von Kármán floor maria (Figs. 2a, 3a and 3b). We suggest the calculated CSFD age of Finsen crater is probably biased by many factors including target properties (different from mare surface), hummocky topography and its effects on mass wasting and crater identification. We refer to the geologic mapping results by Stuart-Alexander (1978) and interpret Finsen it as an Eratoshenian-aged crater.

7. Geologic history of CE-4 landing site and science questions to be answered by Yutu-2

We create a new geologic map of Von Kármán crater region (Fig. 9), which illustrate the regional stratigraphic characteristics and geological evolution history as follows:

1. The South Pole-Aitken basin was formed more than four billion years ago (e.g., Hiesinger et al., 2012; Garrick-Bethell and Miljković, 2018).
2. Multiple large impact craters formed during the post-SPA period, creating a complicated stratigraphic sequence. The impact event that formed the 186-km-diameter Von Kármán crater occurred during the Nectarian period (Ncf: crater floor units, Ncw: crater wall units and Ncrh: hummocky rim units), which has largely destroyed the northern part of the previously formed 245-km-diameter Von Kármán M crater. Then, the 240-km-diameter Leibnitz crater formed north of Von Kármán crater and destroyed part of the northern rim structure of Von Kármán crater and ejected material into the northern part of the Von Kármán crater floor (Ncf units). These ancient, pre-mare crater-related materials are generally characterized by very low FeO and TiO_2 contents, while a slightly more magnesian composition (Fig. 3a, b, c).
3. During the Imbrian period, regional lava-infilling events took place within the SPA basin interior, which generated small mare plains (compared with extensive mare plain within nearside basins), including those within the Von Kármán interior and southern part of the Von Kármán M crater floor (Im1 and Im2: Imbrian mare and Imd: Imbrian dome-like units). The Von Kármán floor surface mare deposits are dated to be ~3.4–3.6 Ga, with buried mare flows to be ~3.7 Ga lava flow at a depth of >100 m. Mare basalts emplaced at the Von Kármán crater floor are characterized by a Ca- and Fe-rich pyroxene composition, with relatively low iron and titanium contents, but relatively higher magnesium.
4. During the post-mare period, the major surface modification processes have been mainly degradation due to ongoing impact cratering, which formed many smaller craters (Ic, Icw, Icr: Imbrian crater materials and Ec: Eratoshenian crater materials). One of most prominent features formed during this period is the Eratoshenian-aged Finsen crater (Ecr: Eratoshenian crater rim materials and Ccw: Eratoshenian crater wall materials), whose ejecta materials extensively overprinted the pre-emplaced mare deposits within Von Kármán crater floor, generating many bright secondary crater chains. These Finsen ejecta materials are characterized by elevated FeO, TiO_2, and LCP content than typical lunar highlands.

Within this geologic context, we propose the following scientific questions related to the traverse and in-situ exploration by the Yutu-2 rover:

1. Composition and origin of nonmare materials. From the landing site, Yutu-2 will be able to measure in-situ the visible and near-infrared spectra of materials mainly composed of Finsen ejecta (perhaps with just a small percentage of basaltic material). To-be-explored questions include: What are the mineral chemistry and assemblage of Finsen ejecta? How much might the surface represent the SPA Composition Anomaly (SPACA) and indicate its origin (Moriarty and Pieters, 2018)? Could Yutu-2 help to find some clues relating to lunar mantle components (i.e., does it contain olivine or Mg-rich LCP)?
2. Composition and origin of lunar farside mare basalts. If Yutu-2 traverses to the west, it will encounter HCP-rich Von Kármán mare basalts. To-be-explored questions include: What are the mineral chemistry and assemblage of these basalts? How do they differ from nearside mare basalts and what are the implications for lunar volcanism?
3. Mixing effects of lunar soils and their evolution. As discussed above, the CE-4 landing site has been greatly affected by post-volcanism impacts. To-be-explored questions include: What's the thickness of nonmare ejecta on basaltic units? What's the variability of soil compositions? Whether the apparent compositional variations are due mainly to contamination of ejecta materials or variations in the basalts?

We believe that Yutu-2 rover will combine information including morphologic (via panorama cameras), mineralogical (via VNIS), and subsurface structures (via LPR), all helping to answer these questions and provide new ground truth for the lunar farside for the first time.

8. Conclusions

We presented a detailed study of the composition, mineralogy, and chronology of basaltic and nonmare materials in Von Kármán crater. Mare basalts in this location have relatively low Fe (13–18 wt% FeO) and low Ti (1–3 wt% TiO_2), and the Mg composition suggests they are relatively high in MgO (~10 wt %) and Mg# (~55). By a spectral survey of 1899 small craters, we derived a mineral (HCP/LCP ratio) map of the region of the landing site, which helps to discriminate the basaltic and

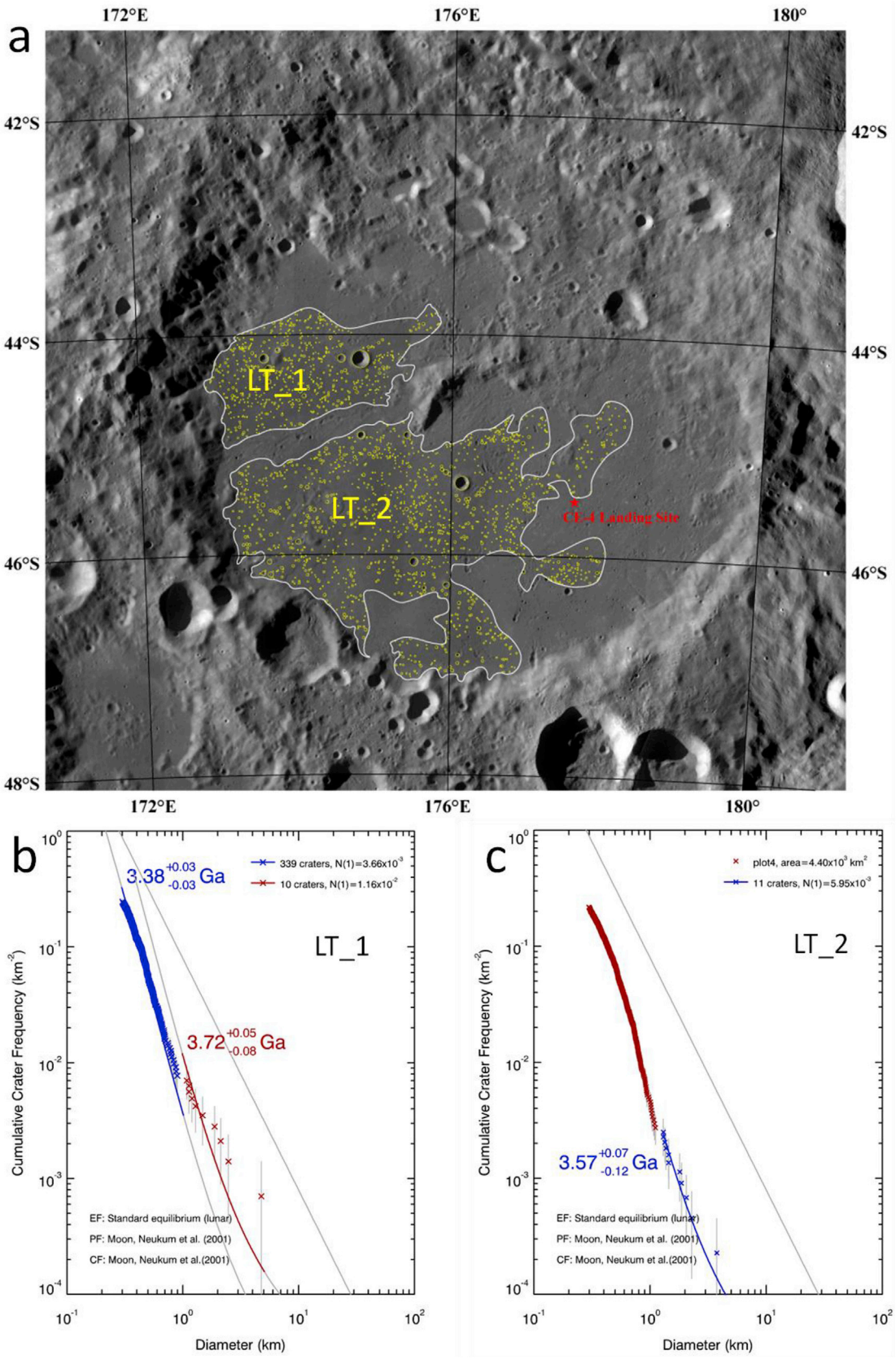


Fig. 8. Chronology of Von Kármán crater basalts and Finsen crater. (a) Locations of crater-counting area for LT unit 1 (LT_1), LT unit 2 (LT_2), yellow points are the counted impact craters >200 m in diameters; (b–c) Chronology result of LT unit 1 and LT unit 2, respectively, based on the Neukum lunar PF and CF, using the CraterStats software package (Michael and Neukum, 2010; Michael et al., 2016). The gray line on the right is the lunar equilibrium function (EF) curve from Trask (1966). (For interpretation of the references to color in this figure legend, the reader is referred to the Web version of this article.)

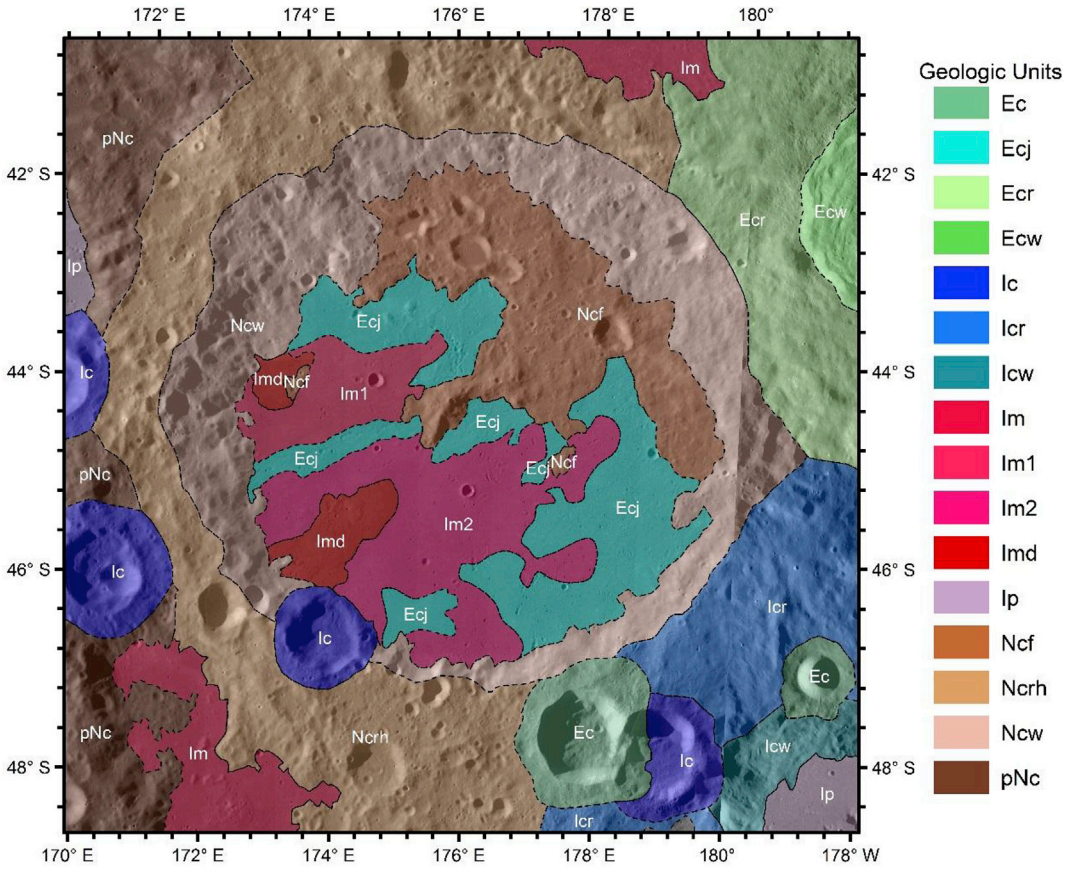


Fig. 9. Geologic map of Von Kármán crater. pNc is pre-Nectarian crater materials, Ncw, Ncrh, Ncf are Nectarian crater wall, hummocky rim, and floor materials, Ip is Imbrian plain materials, Im, Im1 and Im2 are Imbrian mare units, Imd is Imbriaum dome-like unit, Ic is Imbrian materials and can be sub-divided into rim (Icr) and wall (Icw) units, Ec is Eratoshenian crater materials and can be sub-divided into rim (Ecr), wall (Ecw) and ejecta (Ecj) units.

nonmare units by suppressing the upper layer soils mixing and disturbance by impacts and gardening. This region includes nonmare Mg-rich pyroxene materials, nonmare HCP materials, and mare basalts. The nonmare materials are characterized by more magnesian pyroxene compositions compared to the basalts, with Finsen crater material (and its ejecta) more Ca/Fe rich than other parts of the rim of Von Kármán crater. The mare basalts show different reworking and mixing effects. The mixing and evolution of lunar regolith and the layers of mare basalts in this region will benefit from detailed in-situ exploration by the CE-4 rover. In addition, we dated the mare basalts at two model ages of ~3.6 Ga and ~3.4 Ga. We finally draw a new geologic map of this landing region based on above studies, which demonstrate the geologic evolution of landing region and would help to guide the surface roving exploration route of the CE-4 mission.

Our study provides some mineralogical and geological information about the basaltic units in Von Kármán crater. The in-situ analysis of Yutu-2 will help to evaluate the mineral chemistries and subsurface structures in-situ by VNIS and LPR, respectively. We anticipate that the Chang'E−4 mission will bring back new ground truth from the lunar farside surface.

Conflicts of interest

The authors declare there is no conflict of interest for this work.

Acknowledgments

We thank the Editor and three reviewers for their comments and suggestions, which helped us to improve the quality of the manuscript. We also thank Bradley L. Jolliff for for helpful discussions on the geology of CE-4 landing site. This work is supported by the National Natural Science Foundation of China (11941001, 41972322, U1931211 and 41703063), the Natural Science Foundation of Shandong Province (ZR2019MD008), Qilu (Tang) Young Scholars Program of Shandong University, Weihai (2015WHWLJH14), the China Postdoctoral Science Foundation (No. 2017M610421), the Program for JLU Science and Technology Innovative Research Team (JLUSTIRT, 2017TD-26), the Focus on research and development plan in Shandong province (2018GGX101028), the Open Fund of State Key Laboratory of Remote Sensing Science (OFSLRSS201802). All original WAC, SLDEM2015 and M^3 data can be found in the NASA's Planetary Data System (http://pds.nasa.gov/), the original MI data are archived at SELENE Data Archive (https://darts.isas.jaxa.jp/planet/pdap/selene/) and the original IIM data are available from the Data Publishing and Information Service System of China's Lunar Exploration Program (http://moon.bao.ac.cn).

Appendix A. Supplementary data

Supplementary data to this article can be found online at https://doi.org/10.1016/j.pss.2019.104741.

References

Baker, D.M., Head, J.W., Fassett, C.I., Kadish, S.J., Smith, D.E., Zuber, M.T., Neumann, G.A., 2011. The transition from complex crater to peak-ring basin on the Moon: new observations from the Lunar Orbiter Laser Altimeter (LOLA) instrument. Icarus 214, 377–393.

Barker, M., Mazarico, E., Neumann, G., Zuber, M., Haruyama, J., Smith, D., 2016. A new lunar digital elevation model from the lunar orbiter laser altimeter and SELENE terrain camera. Icarus 273, 346–355.

Besse, S., Sunshine, J.M., Staid, M.I., Petro, N.E., Boardman, J.W., Green, R.O., Head, J.W., Isaacson, P.J., Mustard, J.F., Pieters, C.M., 2011. Compositional

variability of the Marius Hill volcanic complex from the Moon mineralogy mapper (M^3). J. Geophys. Res. 116, E6.
Boardman, J.W., Pieters, C.M., Green, R.O., Lundeen, S.R., Varanasi, P., Nettles, J., Petro, N., Isaacson, P., Besse, S., Taylor, L.A., 2011. Measuring moonlight: an overview of the spatial properties, lunar coverage, selenolocation, and related Level 1B products of the Moon Mineralogy Mapper. J. Geophys. Res. 116 https://doi.org/10.1029/2010je003730.
Cheek, L.C., et al., 2011. Goldschmidt crater and the Moon's north polar region: results from the Moon mineralogy mapper (M3). J. Geophys. Res. 116 https://doi.org/10.1029/2010je003702.
Di, K.C., Liu, Z.Q., Liu, B., Wan, W.H., Peng, M., Wang, Y.X., Gou, S., Yue, Z.Y., Xin, X., Jia, M.N., Niu, S.L., 2019. Chang'e-4 lander localization based on multi-source data. J. Remot. Sens. 23 (1), 177–184.
Duke, M., Agee, C., Bogard, D., Carrier, W., Coombs, C., Gaddis, L., Head, J.I., Jolliff, B., Lofgren, G., Papanastassiou, D., Papike, J., Pieters, C., Ryder, G., 2000. South Pole-Aitken basin sample return mission. In: Proceedings of the Fourth International Conference on Exploration and Utilization of the Moon. European Space Agency, ESTEC, Noordwijk.
Fassett, C.I., Head, J.W., Kadish, S.J., Mazarico, E., Neumann, G.A., Smith, D.E., Zuber, M.T., 2012. Lunar impact basins: stratigraphy, sequence and ages from superposed impact crater populations measured from Lunar Orbiter Laser Altimeter (LOLA) data. J. Geophys. Res. Planets 117, E00H06.
Garrick-Bethell, I., Miljković, K., 2018. Age of the Lunar South Pole-Aitken Basin. 49th Lunar and Planetary Science Conference. Lunar and Planetary Institute, The Woodlands, Texas. Abstract #2633.
Garrick-Bethell, I., Zuber, M.T., 2009. Elliptical structure of the lunar South Pole-Aitken basin. Icarus 204, 399–408.
Green, R.O., Pieters, C., Mouroulis, P., Eastwood, M., Boardman, J., Glavich, T., et al., 2011. The Moon Mineralogy Mapper (M^3) imaging spectrometer for lunar science: instrument description, calibration, on-orbit measurements, science data calibration and on-orbit validation. J. Geophys. Res. Planets 116, E00G19.
Haruyama, J., Ohtake, M., Matsunaga, T., Morota, T., Honda, C., Yokota, Y., et al., 2009. Long-lived volcanism on the lunar farside revealed by SELENE terrain camera. Science 323, 905–908.
Hawke, B.R., Blewett, D.T., Lucey, P.G., Smith, G.A., Bell, J.F., Campbell, B.A., Robinson, M.S., 2004. The origin of lunar crater rays. Icarus 170, 1–16.
Head, J.W., Murchie, S.L., Mustard, J.F., Pieters, C., Neukum, G., McEwen, A., Greeley, R., Nagel, E., Belton, M.J.S., 1993. New data from the western limb and far side (Orientale and South Pole-Aitken basins) from the first Galileo flyby. J. Geophys. Res. 98, 17149–171181.
Head, J.W., Fassett, C.I., Kadish, S.J., Smith, D.E., Zuber, M.T., Neumann, G.A., Mazarico, E., 2010. Global distribution of large lunar craters: implications for resurfacing and impactor populations. Science 329, 1504–1507.
Hiesinger, H., Head III, J., Wolf, U., Jaumann, R., Neukum, G., 2002. Lunar mare basalt flow units: Thicknesses determined from crater size-frequency distributions. Geophys. Res. Lett. 29 (8), 89.
Hiesinger, H., van der Bogert, C.H., Pasckert, J.H., Schmedemann, N., Robinson, M.S., Jolliff, B., Petro, N., 2012. New crater size-frequency distribution measurements of the south Pole-Aitken basin. Lunar and Planetary Sci. Conf. 43. Abstract #2863.
Huang, J., Xiao, Z., Flahaut, J., Martinot, M., Head, J., Xiao, X., et al., 2018. Geological characteristics of Von Kármán crater, northwestern South Pole-Aitken Basin: Chang'E-4 landing site region. J. Geophys. Res. Planets 123, 1684–1700.
Ivanov, M.A., Hiesinger, H., van der Bogert, C.H., Orgel, C., Pasckert, J.H., Head, J.W., 2018. Geologic history of the northern portion of the south Pole-Aitken basin on the Moon. J. Geophys. Res.: Planets 123, 2585–2612.
Jolliff, B.L., Shearer, C.K., Papanastassiou, D.A., Liu, Y., the MoonRise Science Team, 2017. Why do we need samples from the Moon's South Pole-Aitken basin and what would we do with them? Lunar Planet. Sci. 48. Abstract #1300.
Kneissl, T., van Gasselt, S., Neukum, G., 2011. Map-projection-independent crater size-frequency determination in GIS environments—new software tool for ArcGIS. Planet. Space Sci 59, 1243–1254.
Lemelin, M., Lucey, P.G., Song, E., Taylor, G.J., 2015. Lunar central peak mineralogy and iron content using the Kaguya Multiband Imager: reassessment of the compositional structure of the lunar crust. J. Geophys. Res. Planets 120, 869–887.
Li, C., Liu, J., Ren, X., Mou, L., Zou, Y., Zhang, H., et al., 2010. The global image of the Moon obtained by the Chang'E-1: data processing and lunar cartography. Sci. China Earth Sci. 53 (8), 1091–1102.
Ling, Z., Jolliff, B.L., Wang, A., Li, C., Liu, J., Zhang, J., et al., 2015. Correlated compositional and mineralogical investigations at the Chang' e-3 landing site. Nat. Commun. 6 (1), 8880.
Lucey, P.G., Blewett, D.T., Jolliff, B.L., 2000. Lunar iron and titanium abundance algorithms based on final processing of Clementine ultraviolet-visible images. J. Geophys. Res. 105 (E8), 20297–20305.
Mazrouei, S., Ghent, R.R., Bottke, W.F., Parker, A.H., Gernon, T.M., 2019. Earth and Moon impact flux increased at the end of the Paleozoic. Science 363, 253.
Melosh, H.J., 1989. Impact Cratering: A Geologic Process. Research Supported by NASA. Oxford University Press, New York. Oxford Monographs on Geology and Geophysics, No. 11.
Melosh, H.J., Kendall, J., Horgan, B., Johnson, B.C., Bowling, T., Lucey, P.G., Taylor, G.J., 2017. South Pole–Aitken basin ejecta reveal the Moon's upper mantle. Geology 45 (12), 1063–1066.
Michael, G.G., Neukum, G., 2010. Planetary surface dating from crater size-frequency distribution measurements: partial resurfacing events and statistical age uncertainty. Earth Planet. Sci. Lett. 294, 223–229.
Michael, G.G., Kneissl, T., Neesemann, A., 2016. Planetary surface dating from crater size-frequency distribution measurements: Poisson timing analysis. Icarus 277, 279–285.
Moriarty III, D.P., Pieters, C.M., 2018. The character of South Pole-Aitken Basin: patterns of surface and subsurface composition. J. Geophys. Res. Planets 123, 729–747.
National Research Council, 2007. The Scientifiic Context for the Exploration of the Moon. National Academies Press, Washington, D.C., p. 120
Neukum, G., Ivanov, B.A., Hartmann, W.K., 2001. Cratering records in the inner solar system in relation to the lunar reference system. Space Sci. Rev. 96, 55–86.
Oberbeck, V., Morrison, R., 1974. Laboratory simulation of the herringbone pattern associated with lunar secondary crater chains. The Moon 9, 415–455.
Ohtake, M., Matsunaga, T., Yokota, Y., Yamamoto, S., Ogawa, Y., Morota, T., et al., 2010. Deriving the absolute reflectance of lunar surface using SELENE (Kaguya) multiband imager data. Space Sci. Rev. 154 (1–4), 57–77.
Otake, H., Ohtake, M., Hirata, N., 2012. Lunar iron and titanium abundance algorithms based on SELENE (Kaguya) Multiband Imager data. Lunar and Planetary Sci. Conf. 43rd. Abstract 1905.
Papike, J.J., Ryder, G., Shearer, C.K., 1998. Lunar samples (Ch. 5). In: Papike, J.J. (Ed.), Planetary Materials. Mineralogical Society of America, Washington, D.C., USA, pp. 1–234.
Pasckert, J.H., Hiesinger, H., van der Bogert, C.H., 2018. Lunar farside volcanism in and around the South Pole–Aitken basin. Icarus 299, 538–562.
Pieters, C.M., Hanna, K.D., Cheek, L., Dhingra, D., Prissel, T., Jackson, C., et al., 2014. The distribution of Mg-spinel across the Moon and constraints on crustal origin. Am. Mineral. 99 (10), 1893–1910.
Prettyman, T.H., Hagerty, J.J., Elphic, R.C., Feldman, W.C., Lawrence, D.J., Mckinney, G.W., Vaniman, D.T., 2006. Elemental composition of the lunar surface: analysis of gamma ray spectroscopy data from Lunar Prospector. J. Geophys. Res. Planets 111, E12007.
Qiao, L., Ling, Z., Fu, X., Li, B., 2019. Geological characterization of the Chang'e-4 landing area on the lunar farside. Icarus 333, 37–51.
Ravi, S., Mahanti, P., Meyer, H., Robinson, M.S., 2016. On the Usefulness of Optical Maturity for Relative Age Classification of Fresh Craters. American Geophysical Union Fall Meeting, San Francisco, California abstract #P53A-2166.
Robinson, M.S., Brylow, S.M., Tschimmel, M., Humm, D., Lawrence, S.J., Thomas, P.C., et al., 2010. Lunar reconnaissance orbiter camera (LROC) instrument overview. Space Sci. Rev. 150 (1–4), 81–124.
Shoemaker, E.M., 1962. Interpretation of lunar craters. In: Kopal, Z. (Ed.), Physics and Astronomy of the Moon. Academic Press, New York, pp. 283–360.
Smith, D.E., Zuber, M.T., Neumann, G.A., Lemoine, F.G., Mazarico, E., Torrence, M.H., et al., 2010. Initialobservations from the lunar orbiter laser altimeter (LOLA). Geophys. Res. Lett. 37, L18204.
Stuart-Alexander, D.E., 1978. Geologic Map of the Central Far Side of the Moon. U.S. Geol. Surv., Map I-1047, Reston, VA.
Sunshine, J.M., Pieters, C.M., 1993. Estimating modal abundances from the spectra of natural and laboratory pyroxene mixtures using the modified Gaussian model. J. Geophys. Res. 98, 9075–9087.
Sunshine, J.M., Pieters, C.M., 1998. Determining the composition of olivine from reflectance spectroscopy. J. Geophys. Res. 103, 13675–13688.
Thiessen, F., Besse, S., Staid, M.I., Hiesinger, H., 2014. Mapping lunar mare basalt units in mare Imbrium as observed with the Moon Mineralogy Mapper (M^3). Planet. Space Sci. 104, 244–252.
Trask, N.J., 1966. Size and spatial distribution of craters estimated from the Ranger photographs. Jet Propul. Lab. Tech. Rep., 32–700 Pasadena, California, pp. 252–263.
Werner, S.C., Medvedev, S., 2010. The Lunar rayed-crater population - characteristics of the spatial distribution and ray retention. Earth Planet. Sci. Lett. 295, 147–158.
Wilhelms, D.E., 1987. The Geologic History of the Moon. U.S. Geol. Surv. Prof. Pap. 1348.
Wu, W.R., Wang, Q., Tang, Y.H., Yu, G.B., Liu, J.Z., Zhang, W., et al., 2017. Design of Chang'E-4 lunar farside soft-landing mission (in Chinese). Journal of Deep Space Explor. 4 (2), 111–117.
Yamamoto, S., Nakamura, R., Matsunaga, T., Ogawa, Y., Ishihara, Y., Morota, T., et al., 2012. Olivine-rich exposures in the south Pole-Aitken basin. Icarus 218 (1), 331–344.
Yingst, R., Chuang, F., Berman, D., Mest, S., 2017. Geologic mapping of the planck quadrangle of the Moon (LQ-29). Lunar Planet. Sci. 48. Abstract #1680.